ROYAL SOCIETY
OF CHEMISTRY

PAPER

Check for updates

Atomic ribbon formation in the pulsed laser patterning of WS$_2$ layers

Yaowu Hu, [ID] *[a,b,c] Zifeng Wang,[b] Zequn Zhang[b] and Jie Guan [ID] [d]

The precise modulation of the thickness of two-dimensional (2D) semiconductor transition metal disulfides (TMDs) by laser thinning techniques to tailor their electronic properties is recognized as a promising approach. However, achieving sub-diffractive patterning during layer-by-layer modulation is crucial for junction fabrication and device engineering. Herein, we report atomic nanoribbon generation in single-layer tungsten disulfide (WS$_2$), namely, the atomic laser-induced periodic surface structure (atomic-LIPSS) effect, achieved by tuning the laser pulse width, energy and other processing parameters. We explore the structural evolution of WS$_2$ during laser processing for monolayer and multilayer films and compare it with another more commonly encountered 2D material, MoS$_2$. It is verified experimentally and by molecular dynamics simulations (MD) that such atomic nanoribbons can only be formed under the action of short-pulse (<ns) lasers.

Introduction

Since the successful stripping of monolayer graphene,[1] two-dimensional (2D) materials have attracted much attention. Transition metal disulfides (TMDs), which also have atomic-level thickness, are of interest due to their large number of interesting physical properties, ranging from optical nonlinearity[2] and magnetism[3] to superconductivity.[4] These physical properties arise from their compositional tunability, where the desired electrical and optical properties are achieved by varying the combination of transition metals and sulfur groups, and there are about 40 different types of TMDs.[5] Interestingly, different TMDs stacked together can almost form new materials by generating new shared exciton states[6] and charge separation at the femtosecond scale.[7] WS$_2$, as an important member of the TMDs family, has a bandgap that varies according to its thickness, from direct bandgap of 2.05 eV for its single layer to indirect bandgaps for its multiple layers.[8] WS$_2$ also has several interesting properties, such as an excellent on–off ratio (4×10^6), strong spin–orbit coupling,[9] high valley polarization,[10] and other properties.[11–13] The excellent optical and electrical properties of monolayer WS$_2$ are important for the development of electronic devices.

Currently, chemical vapor deposition (CVD) has been shown to grow high-quality continuous monolayers of WS$_2$ with sizes of hundreds of micrometers, and it is the most promising method for large-scale applications.[14] The patterning of these materials remains challenging due to the atomic thickness.[15] Current patterning techniques include electron-beam patterning,[16] chemical patterning,[17] optical patterning,[18–20] imprint lithography[21] and inkjet printing.[22,23] While LIPSS structures[24–26] are found in laser-bulk matter interactions, atomic nanoribbons from two-dimensional materials have never been reported before.

In this work, we obtained atomic nanoribbons of 2D-WS$_2$ thin films through the LIPSS effect based on laser processing methods under different pulse widths and energy conditions. By combining density functional theory (DFT) calculations, MD simulations, and experimental characterization using scanning electron microscopy (SEM), the thermal diffusion changes of pulsed lasers in different environments and the formation mechanism of atomic nanoribbons were explored and analyzed. FDTD calculations analyzed the performance of nanoribbons with different thicknesses and structures in the optical field. Finally, we prepared a monolayer WS$_2$ containing atomic nanoribbons for gas sensors and demonstrated good performance.

*a*School of Integrated Circuits, Wuhan University, Wuhan, 430072, China
*b*The Institute of Technological Sciences, Wuhan University, Wuhan, 430072, China. E-mail: yaowuhu@whu.edu.cn; Tel: +86-13387587827
*c*School of Power and Mechanical Engineering, Wuhan University, Wuhan, 430072, China
*d*School of Physics, Southeast University, Nanjing, 211189, China

Materials and methods

A monolayer of WS$_2$ was prepared on a sapphire substrate by the CVD method. Sodium tungstate (Na$_2$WO$_4$) solution was first used as a tungsten source for spin-coating on the sapphire

substrate, whereas the S vapors were transported to the substrate *via* a mixed carrier gas of Ar/H$_2$ to react with the tungsten source. Fig. S1a shows a monolayer of WS$_2$ prepared by CVD, where all the bright yellow areas represent WS$_2$ and dark yellow represents the sapphire substrate, which was transferred onto a Si substrate by a wet transfer technique in order to easily differentiate the substrate from WS$_2$. The transfer steps are detailed in the SI. In this case, the substrate was covered with a 300 nm oxide layer. Fig. S1b is a picture of WS$_2$ on a silicon substrate, where the light-yellow area is SiO$_2$ and the dark yellow area is a monolayer of WS$_2$. An optical microscope was used for observation, and the objective lenses used were 50× and 100×. Fig. S4e shows the thickness of WS$_2$ measured by AFM, which is about 0.82 nm, consistent with the literature.[27] Fig. S1c and S1d show the Raman and PL spectra of WS$_2$ in this area, and the results indicate that WS$_2$ is a monolayer.[28] A 100× objective lens was used to measure the Raman and PL spectra. The laser excitation wavelength used was 532 nm with an energy of less than 0.5 mW to avoid thermal damage.

The laser wavelength used in the manufacturing process was 1060 nm, and the pulse widths were 190 fs and 350 ns. The thermal effects of other pulse width conditions and different laser powers on the monolayer WS$_2$ were simulated using the LAMMPS MD software. The energy band structure of WS$_2$ was calculated by DFT. Detailed descriptions of the MD and DFT methods are given in the SI. The electric field distribution and light absorption of different atomic nanobelt structures were calculated using FDTD.

Results and discussion

During the machining of the monolayer WS$_2$ using pulsed laser subtractive machining, different pulse widths and energies lead to different machining results. As shown in Fig. 1a, WS$_2$ produces laser-induced periodic surface structure (LIPSS) on the atomic scale when a short-pulse laser is applied. This structure is produced by the polarization effect of the laser (Fig. S2) and varies with the power of the laser. When the power of the laser is low, this structure appears as atomic nanoribbons, and when the power of the laser is increased, the atomic nanoribbons disappear in favor of jagged boundaries on both sides of the machining area. This is the first time that the LIPSS effect has been observed on the atomic scale.

Fig. 1b and d show the SEM images of single-layer WS$_2$ processed with a 350 ns pulsed laser, and Fig. 1c and e show the SEM images of single-layer WS$_2$ processed with a 190 fs pulsed laser. The laser energy is 0.6 mW in Fig. 1b and c, and 1 mW in Fig. 1d and e. Under the irradiation of the femtosecond laser energy of 0.6 mW, the processed region of WS$_2$ produced atomic nanoribbons in the LIPSS effect, and the processed boundaries were neater. The nanosecond laser at low energy level produced partial removal effect with a fraction of debris left in the processed area.

Raman and PL spectra were obtained in the machining area and near the boundaries of the two pulsed lasers mentioned above, and the results are shown in Fig. 1f–i, respectively. The
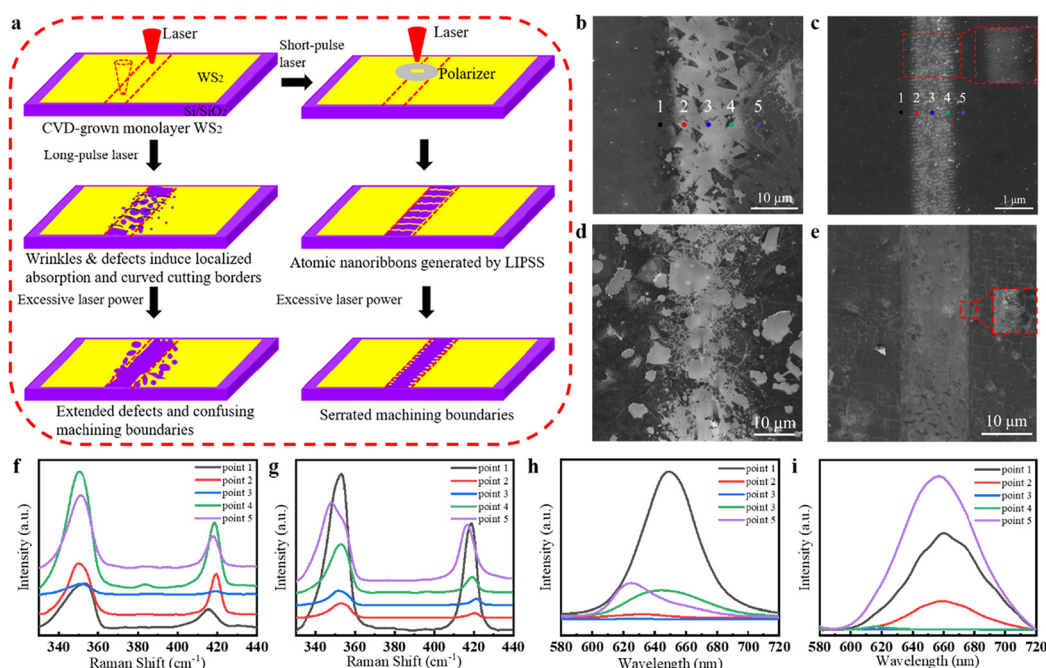

Fig. 1 Pulsed laser subtractive manufacturing process of the CVD-grown monolayer WS$_2$ and results of femtosecond and nanosecond laser machining. (a) Schematic of the monolayer WS$_2$ machined by different pulsed laser subtractive machining. SEM images of the monolayer WS$_2$ for subtractive machining using (b) 350 ns and (c) 190 fs pulsed lasers. SEM images of the monolayer WS$_2$ for subtractive machining using a (d) nanosecond laser and (e) femtosecond laser at excessive energies. (f), (g) Raman spectra and (h), (i) PL spectra for the laser-subtracted machining of the monolayer WS$_2$ with 350 ns (left) and 190 fs (right) pulsed lasers.

five measured curves correspond to the five points in Fig. 1b and c. It can be clearly seen that after nanosecond laser machining, the Raman peak in the machined area shifted drastically, and the PL spectrum underwent an obvious blue shift. This indicates that after nanosecond laser machining, the WS_2 in the machined area had large defects and was strained by the laser thermal effect.[29] After femtosecond laser machining, the peak of the Raman spectrum in the machined area did not shift significantly, and the PL spectrum was not shifted. This suggests that there was still some residue of WS_2 in the machined area after femtosecond laser machining, indicating the LIPSS nanoribbons. The straining effect of WS_2 under the action of the femtosecond laser was not obvious.

MD simulations were performed to investigate the thermal distribution and wrinkle changes during laser machining of WS_2 at different pulse widths. Fig. 2a shows a cloud view of the temperature distribution of the whole monolayer WS_2 when the machining area was heated up to a certain temperature by lasers of different pulse widths. It was found that when the pulse width is larger, the high-temperature area becomes larger. On the contrary, when the pulse width is small, the heat transfer in WS_2 is weaker, providing the necessary conditions for the formation of atomic nanoribbons in LIPSS.

Fig. 2b shows the spatial distribution of the temperature field in the monolayer WS_2 for three pulse width conditions.

Fig. 2c shows a cloud plot of the height distribution of thermally deformed WS_2 for different pulse widths. As the pulse width increased, wrinkles appeared in WS_2 and progressively widened and strengthened. As shown in Fig. 2d and e, for the wrinkle-free monolayer WS_2, the calculated initial bandgap widths are in agreement with other reports.[30] When wrinkles are introduced, the bandgap of WS_2 decreases with the increase in wrinkle height, which enhances the interaction between the laser and the WS_2 layer, creating more defects near the machining area and inhibiting the formation of atomic nanoribbons.

The effects of the laser processing of the monolayer WS_2 at different pulse widths and energies were simulated using MD and compared with the previously calculated results for MoS_2. As MoS_2 is widely used as an atomic crystal in literature, and it has a similar structure to WS_2, this paper presents the simulation results of MoS_2 in comparison with WS_2. In Fig. 3a, the red rectangular box shows the laser action area. It can be seen that as the pulse width of the laser increases, the removal region expands. Fig. 3b shows that as the total energy increased, the number of atoms removed by the laser increased (Fig. S2). Fig. 3c and d show the material removal
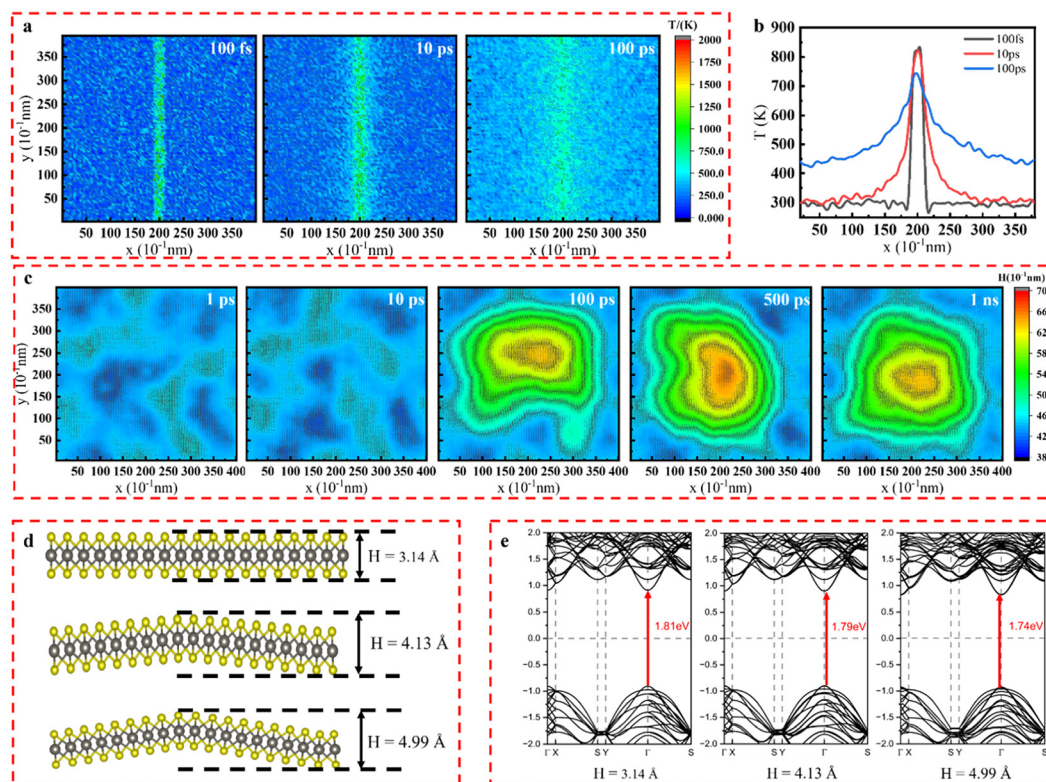

Fig. 2 Thermal transfer of WS_2 by laser machining with different pulse widths and the effect of wrinkles generated during machining on the energy bands. (a) Temperature distribution of the monolayer WS_2 during laser processing with different pulse widths. (b) Spatial distribution of the temperature field under different pulse width conditions. (c) Cloud map of the wrinkle altitude distribution of the monolayer WS_2 generated by laser subtractive machining with different pulse widths. (d) Schematic of the monolayer WS_2 at different wrinkle heights. (e) Energy band structure of monolayer WS_2 at different wrinkle heights.
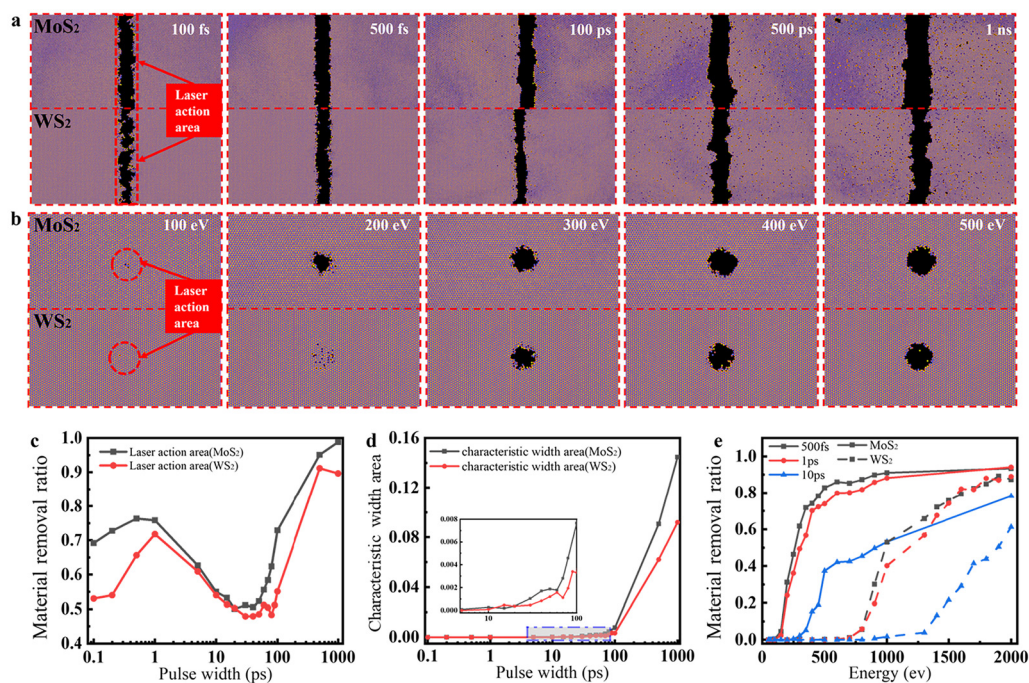
Fig. 3 Comparison of MD simulation results for laser machining of the monolayer MoS_2 and WS_2 under different pulse widths and energies. (a) Comparison of MD-simulated laser machining of the monolayer MoS_2 and WS_2 at different pulse widths. (b) Comparison of MD-simulated laser machining of the monolayer MoS_2 and WS_2 using a 500 fs pulsed laser at different power levels. (c) Material removal ratio of MoS_2 and WS_2 in the laser action region as a function of the laser pulse width. (d) Characteristic width area of MoS_2 and WS_2 as a function of laser pulse width. (e) Material removal ratio of MoS_2 and WS_2 in the laser action region as a function of laser energy for the three selected pulse widths. Dashed lines for WS_2. Solid lines for MoS_2.
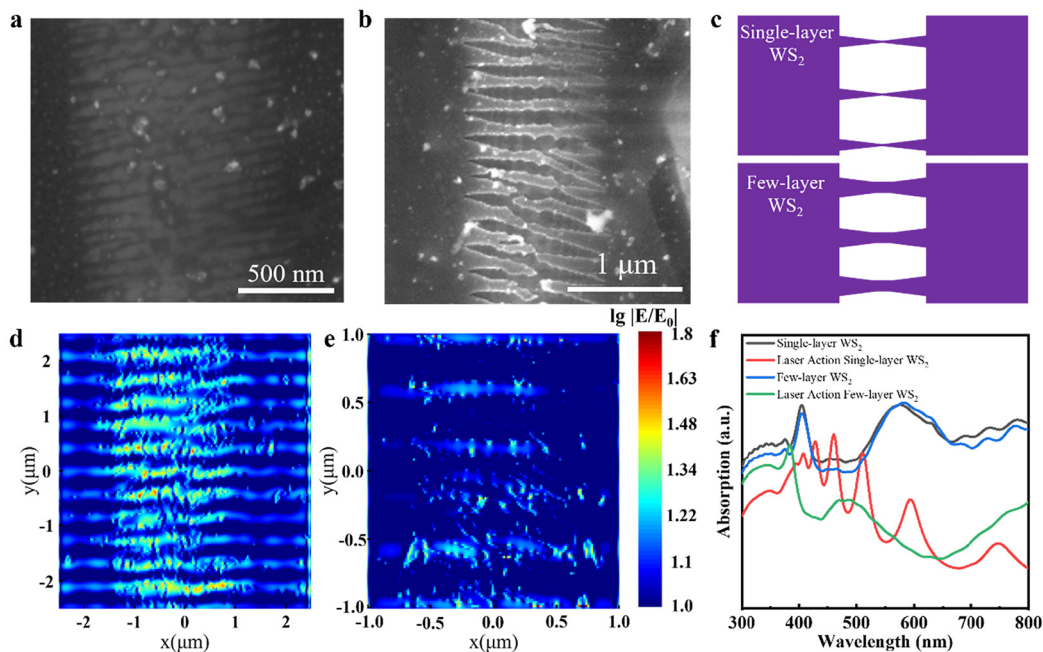

Fig. 4 LIPSS structure formed with different numbers of layers of WS_2. (a) SEM images of the LIPSS structure of a (a) single-layer WS_2 and (b) few-layer WS_2. (c) Schematic of the LIPSS structural model of single-layer and few-layer WS_2. Electric field distribution of LIPSS structures with a (d) single-layer WS_2 and (e) few-layer WS_2. (f) Effects of single-layer WS_2 and few-layer WS_2 LIPSS structures on light absorption.

ratios of WS_2 and MoS_2 atoms in the laser action area and the characteristic width area, respectively, for different pulse widths. It can be seen that for both WS_2 and MoS_2, when the pulse width is less than 1 ps, the atomic loss ratio in the laser action area increases with the increase in the pulse width. When the pulse width is between 1 ps and 40 ps, the atomic loss ratio in the laser action area decreases with the increase in the pulse width. The characteristic length generally increases with pulse width (Fig. 3d). Fig. 3e shows the material removal ratio as a function of energy for three pulse widths. As the laser pulse width increases, the threshold energy for laser

removal of WS_2 and MoS_2 increases, and it is more difficult to remove the atoms from WS_2 than from MoS_2. This may be due to the fact that the thermal conductivity of MoS_2 is lower than that of WS_2.

In order to investigate the influence of the number of layers on the LIPSS effect, the few-layer WS_2 was subtractively machined using a femtosecond laser, and the results are shown in Fig. 4. It was observed that different numbers of layers led to different atomic nanoribbons produced by LIPSS. When WS_2 is single-layer, the atomic nanoribbons are mainly dominated by two symmetric triangles with one corner being
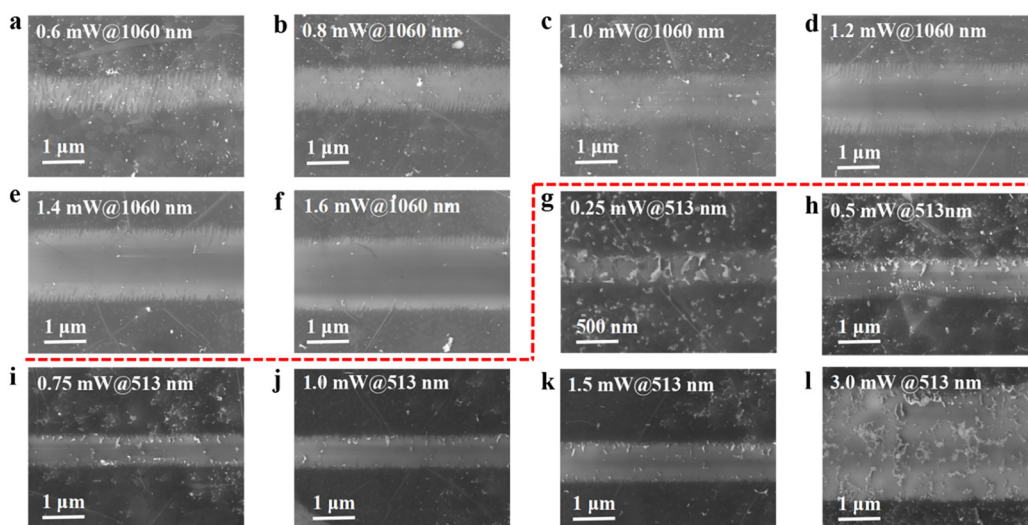

Fig. 5 Periodic structures produced by the subtractive fabrication of atomic layers of WS_2 using lasers of different wavelengths and energies. (a)–(f) The laser wavelength is 1060 nm. (g)–(l) The laser wavelength is 513 nm.
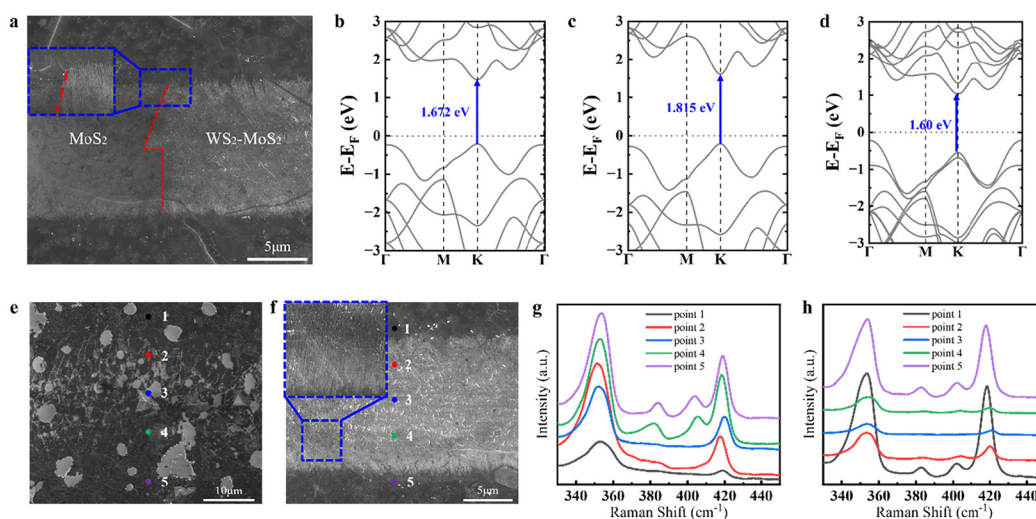

Fig. 6 Results of the laser processing of the WS_2–MoS_2 heterojunction. (a) SEM image of the femtosecond laser-processed WS_2–MoS_2 heterojunction. Energy band structures of the (b) monolayer WS_2, (c) monolayer MoS_2 and (d) the WS_2–MoS_2 heterojunction calculated from DFT. SEM images of the WS_2–MoS_2 heterojunction machined using the 350 ns (e) and 190 fs (f) lasers. Raman spectra of the WS_2–MoS_2 heterojunction machined by the nanosecond (g) and femtosecond (h) laser.

adjacent. In contrast, the atomic nanoribbons produced by few-layer WS_2 under the action of femtosecond laser are dominated by two connecting trapezoids, and the width of the atomic nanoribbons is much larger than that of the single-layer WS_2. We provide SEM images of coexisting single-layered and multilayered WS_2 films *via* femtosecond laser scanning in Fig. S3. The differences are attributed to heat transfer and light absorption effects, as shown in Fig. 4(d–f).

By changing the energy and wavelength of the femtosecond laser, it was found that the atomic-level LIPSS will change. The SEM results in Fig. 5a–f show that when the laser wavelength is 1060 nm, with the increase in laser energy (0.6 mW– 1.6 mW), the laser-actuated area gradually breaks from the original atomic nanoribbon and forms a sawtooth structure at the edge. As shown in Fig. 5g–l, when the laser wavelength was tuned to 513 nm, the LIPSS effect was still present but not obvious. MoS_2 does not appear to have similar LIPSS structures under the same laser conditions.

In order to investigate whether WS_2 can generate atomic nanoribbons in stacked materials, a WS_2–MoS_2 heterojunction was built by the wet transfer technique. The specific steps are shown in Fig. S4. The stacked material and the single-layer MoS_2 region were processed using a femtosecond laser with a laser power of 0.8 mW. The results are shown in Fig. 6a. Atomic nanoribbons can be clearly seen for areas with WS_2. From DFT analysis in Fig. 6b–d, the bandgap of the stacked material is smaller than that of the monolayer WS_2. In order to investigate the material residuals of the stacked materials after nanosecond and femtosecond laser processing, Raman spectroscopy measurements were carried out on the regions after processing. Only WS_2 was found remaining in the stacked material after femtosecond laser processing. In contrast, after nanosecond laser processing, both MoS_2 and WS_2 were detected in the processed region, and irregular defects were generated near the processed region. This result shows the differences between the patterning of MoS_2 and WS_2.

Conclusion

Herein, we investigated the pattern formation mechanism in 2D-WS_2 using a pulsed laser with different laser parameters. The results show that as the laser pulse width increases, the heat transfer time increases and deformation, thermal cracks and other complex morphologies appear at the boundary of the laser removal region. Atomic LIPSS nanoribbons were first observed in the ultrafast laser irradiation of single-layer WS_2. The experimental results were analyzed along with MD simulations. The structure of the atomic nanoribbons generated by the LIPSS effect is affected by the number of WS_2 layers, and FDTD calculations show that the atomic nanoribbons generated with different layers have different light absorption performances, providing a new idea for the laser patterning of 2D materials. The results of this paper are useful for understanding the complex phenomenon of intense light–matter interactions in WS_2 and promoting the application of WS_2 devices.

Author contributions

The manuscript is written with contributions from all authors. All the authors approved the final version of the manuscript.

Conflicts of interest

The authors declare that they have no known competing financial interests or personal relationships that could have appeared to influence the work reported in this paper.

Data availability

Data will be made available on request.

Supplementary information (SI) is available. The data includes more details of experimental and simulation methods, characterizations of our CVD grown WS_2, SEM of atomic LIPSS with different femto-laser scan paths, coexisting multi-layer and monolayer WS_2 with femto-laser irradiation, and spot femto-laser irradiation of monolayer WS_2 at different powers. See DOI: https://doi.org/10.1039/d5nr03677a.

Acknowledgements

References

1 K. S. Novoselov, A. K. Geim, S. V. Morozov, D. Jiang, Y. Zhang, S. V. Dubonos, I. V. Grigorieva and A. A. Firsov, *Electric Field Effect in Atomically Thin Carbon Films*, Kluwer, 2000, vol. 306.

2 X. Wen, Z. Gong and D. Li, *InfoMat*, 2019, **1**, 317–337.

3 B. Scharf, G. Xu, A. Matos-Abiague and I. Žutić, *Phys. Rev. Lett.*, 2017, **119**, 1–6.

4 Y.-T. Hsu, A. Vaezi, M. H. Fischer and E.-A. Kim, *Nat. Commun.*, 2017, **8**, 14985.

5 D. Jariwala, V. K. Sangwan, L. J. Lauhon, T. J. Marks and M. C. Hersam, *ACS Nano*, 2014, **8**, 1102–1120.

6 X. Zhu, J. He, R. Zhang, C. Cong, Y. Zheng, H. Zhang, S. Wang, H. Zhao, M. Zhu, S. Zhang, S. Li and L. Chen, *Nano Res.*, 2022, **15**, 2674–2681.

7 C. Lee, G. Lee, A. M. Van Der Zande, W. Chen, Y. Li, M. Han, X. Cui, G. Arefe, C. Nuckolls, T. F. Heinz, J. Guo, J. Hone and P. Kim, *Nat. Nanotechnol.*, 2014, **9**, 676–681.

8 H. R. Gutiérrez, N. Perea-López, A. L. Elías, A. Berkdemir, B. Wang, R. Lv, F. López-Urías, V. H. Crespi, H. Terrones and M. Terrones, *Nano Lett.*, 2013, **13**, 3447–3454.

9 D. W. Latzke, W. Zhang, A. Suslu, T. R. Chang, H. Lin, H. T. Jeng, S. Tongay, J. Wu, A. Bansil and A. Lanzara, *Phys. Rev. B: Condens. Matter Mater. Phys.*, 2015, **91**, 1–6.

10 A. T. Hanbicki, K. M. McCreary, G. Kioseoglou, M. Currie, C. S. Hellberg, A. L. Friedman and B. T. Jonker, *AIP Adv.*, 2016, **6**, 055804.

11 F. Gong, W. Luo, J. Wang, P. Wang, H. Fang, D. Zheng, N. Guo, J. Wang, M. Luo, J. C. Ho, X. Chen, W. Lu, L. Liao and W. Hu, *Adv. Funct. Mater.*, 2016, **26**, 6084–6090.

12 L. Yang, K. Majumdar, H. Liu, Y. Du, H. Wu, M. Hatzistergos, P. Y. Hung, R. Tieckelmann, W. Tsai, C. Hobbs and P. D. Ye, *Nano Lett.*, 2014, **14**, 6275–6280.

13 H. M. W. Khalil, M. F. Khan, J. Eom and H. Noh, *ACS Appl. Mater. Interfaces*, 2015, **7**, 23589–23596.

14 W. Yang, Y. Mu, X. Chen, N. Jin, J. Song, J. Chen, L. Dong, C. Liu, W. Xuan, C. Zhou, C. Cong, J. Shang, S. He, G. Wang and J. Li, *Discover Nano*, 2023, **18**, 13.

15 Y. Liu, X. Duan, H. Shin, S. Park, Y. Huang and X. Duan, *Nature*, 2021, **591**, 43–53.

16 F. Zheng, D. Guo, L. Huang, L. W. Wong, X. Chen, C. Wang, Y. Cai, N. Wang, C. Lee, S. P. Lau, T. H. Ly, W. Ji and J. Zhao, *Adv. Sci.*, 2022, **9**, 2200702.

17 A. J. Way, R. M. Jacobberger and M. S. Arnold, *Nano Lett.*, 2018, **18**, 898–906.

18 P. S. Kollipara, J. Li and Y. Zheng, *Research*, 2020, **2020**, 1–10.

19 C. Gong, K. Hu, X. Wang, P. Wangyang, C. Yan, J. Chu, M. Liao, L. Dai, T. Zhai, C. Wang, L. Li and J. Xiong, *Adv. Funct. Mater.*, 2018, **28**, 1706559.

20 Z. Wang, Z. Huang, N. Lu, J. Guan and Y. Hu, *Int. J. Heat Mass Transfer*, 2023, **204**, 123873.

21 H. Gao, Y. Hu, Y. Xuan, J. Li, Y. Yang, R. V. Martinez, C. Li, J. Luo, M. Qi and G. J. Cheng, *Science*, 2014, **346**, 1352–1356.

22 O. Song, D. Rhee, J. Kim, Y. Jeon, V. Mazánek, A. Söll, Y. A. Kwon, J. H. Cho, Y. H. Kim, Z. Sofer and J. Kang, *npj 2D Mater. Appl.*, 2022, **6**, 1–12.

23 G. Hu, L. Yang, Z. Yang, Y. Wang, X. Jin, J. Dai, Q. Wu, S. Liu, X. Zhu, X. Wang, T. C. Wu, R. C. T. Howe, T. Albrow-Owen, L. W. T. Ng, Q. Yang, L. G. Occhipinti, R. I. Woodward, E. J. R. Kelleher, Z. Sun, X. Huang, M. Zhang, C. D. Bain and T. Hasan, *Sci. Adv.*, 2020, **6**, 1–6.

24 J. Bonse, S. V. Kirner and J. Krüger, in *Handbook of Laser Micro- and Nano-Engineering*, Springer International Publishing, Cham, 2021, pp. 1–59.

25 E. L. Gurevich, *Appl. Surf. Sci.*, 2016, **374**, 56–60.

26 P. Gregorčič, M. Sedlaček, B. Podgornik and J. Reif, *Appl. Surf. Sci.*, 2016, **387**, 698–706.

27 C. Lan, Z. Zhou, Z. Zhou, C. Li, L. Shu, L. Shen, D. Li and R. Dong, *Nano Res.*, 2018, **11**, 3371–3384.

28 S. Li, S. Wang, D. Tang, W. Zhao, H. Xu and L. Chu, *Appl. Mater. Today*, 2015, **1**, 60–66.

29 F. Wang, S. Li, M. A. Bissett, I. A. Kinloch, Z. Li and R. J. Young, *2D Mater.*, 2020, **7**, 2–4.

30 C. Poornimadevi, C. Preferencial Kala and D. J. Thiruvadigal, *Mater. Sci. Semicond. Process.*, 2023, **157**, 107339.